

Cross-Scale Pansharpening via ScaleFormer and the PanScale Benchmark

Ke Cao^{1,2,*}, Xuanhua He^{3,*†}, Xueheng Li^{1,2}, Lingting Zhu⁴, Yingying Wang⁵,
Ao Ma⁶, Zhanjie Zhang⁷, Man Zhou^{2,‡}, Chengjun Xie^{1,2}, Jie Zhang^{1,2,‡}

¹HFIPS, Chinese Academy of Sciences, ²University of Science and Technology of China,

³The Hong Kong University of Science and Technology, ⁴The University of Hong Kong,

⁵Xiamen University, ⁶JD.com, ⁷Zhejiang University

{caoke200820, hexuanhua, manman}@mail.ustc.edu.cn, zhangjie@iim.ac.cn

Abstract

Pansharpening aims to generate high-resolution multi-spectral images by fusing the spatial detail of panchromatic images with the spectral richness of low-resolution MS data. However, most existing methods are evaluated under limited, low-resolution settings, limiting their generalization to real-world, high-resolution scenarios. To bridge this gap, we systematically investigate the data, algorithmic, and computational challenges of cross-scale pansharpening. We first introduce PanScale, the first large-scale, cross-scale pansharpening dataset, accompanied by PanScale-Bench, a comprehensive benchmark for evaluating generalization across varying resolutions and scales. To realize scale generalization, we propose ScaleFormer, a novel architecture designed for multi-scale pansharpening. ScaleFormer reframes generalization across image resolutions as generalization across sequence lengths: it tokenizes images into patch sequences of the same resolution but variable length proportional to image scale. A Scale-Aware Patchify module enables training for such variations from fixed-size crops. ScaleFormer then decouples intra-patch spatial feature learning from inter-patch sequential dependency modeling, incorporating Rotary Positional Encoding to enhance extrapolation to unseen scales. Extensive experiments show that our approach outperforms SOTA methods in fusion quality and cross-scale generalization. The datasets and source code are available upon acceptance.

1. Introduction

High-resolution multi-spectral (HRMS) imagery is in high demand across various fields such as environmental monitoring and precision agriculture, due to its ability to provide

* Equal contribution.

† Project leader.

‡ Corresponding author.

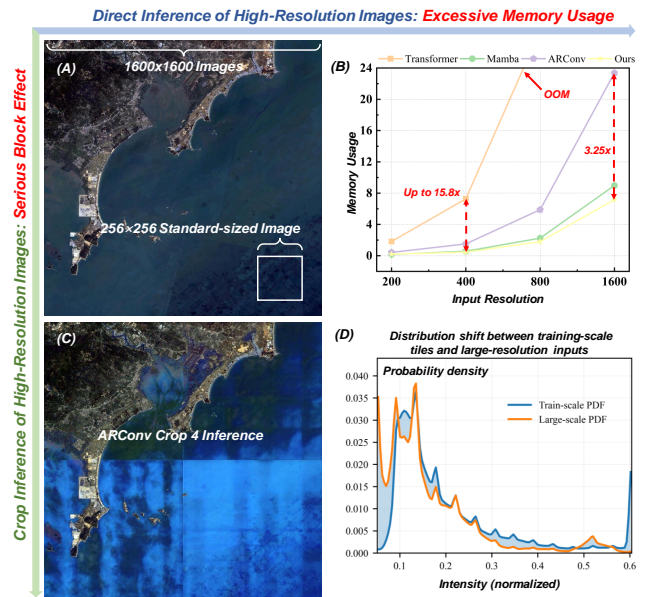


Figure 1. Challenges in cross-scale pansharpening. (a) Learning/modeling at limited resolution while supporting inference on high-resolution images. (b) GPU memory increases rapidly with resolution, especially for Transformer-based models. (c) Tiled inference can introduce block artifacts in some methods. (d) A scale-induced distribution shift exists between training-scale inputs and large-scale inference.

fine spatial detail and rich spectral information. However, current remote sensing technologies face fundamental limitations of satellite sensor hardware, making it difficult to acquire HRMS images directly. As a result, existing systems typically capture high-resolution panchromatic (PAN) images that contain fine spatial detail, alongside low-resolution multi-spectral (LRMS) images that preserve spectral characteristics. To overcome this constraint, pansharpening has been developed to utilize PAN and LRMS images to generate a fusion that combines the advantages of both. Essentially,

pansharpening can be viewed as a guided super-resolution process, where the fine-grained spatial details from the PAN are leveraged to enhance the LRMS while preserving its spectral fidelity. Despite recent advances in CNN- and Transformer-based pansharpening [38, 44, 53, 56, 57] have shown promising progress, they still face several challenges, particularly in handling images with high spatial resolutions and across varying scales. These limitations hinder their generalization and robustness in real-world applications involving multi-scale or high-resolution data.

In practical remote-sensing deployments, inference is typically performed at resolutions far exceeding the training crop size, which exposes two fundamental bottlenecks in existing approaches. **First, computation and memory scale steeply with input size:** when moving from common training crops (200-256 pixels) to 800, 1600, or even 2000 pixels kernel coverage, feature-map dimensions, and attention sequence length increase in lockstep, leading to a sharp rise in computational cost. Engineers are then forced to adopt tiled inference, which introduces boundary discontinuities and visible blocking artifacts. As illustrated in Fig. 1(a) and (b), panel (a) contrasts a typical training crop with our 1600-pixel inference image, while panel (b) shows the sharp rise in memory consumption with increasing resolution, particularly for Transformer-based models, which often exceed consumer-grade GPU capacity already at 800-pixel inputs. Fig. 1(c) highlights severe block artifacts observed with AR-Conv [44] under tiled inference, leading to a marked drop in fusion quality. **Second, cross-scale generalization is weak:** because most models are trained on a single, low-resolution regime, upscaling at test time induces pronounced shifts in input statistics (means, variances, and spectral composition) relative to the training distribution, degrading feature alignment and spectral fidelity and thus causing systematic performance decline [6]. To quantify this scale-induced shift, we compare pixel PDFs between training-scale tiles and large-scale inference. As resolution increases from 200 to 1600, the luminance distribution exhibits systematic shifts in shadows and highlights, which substantially impact fusion quality. **Compounding these issues is the lack of standardized datasets and evaluation protocols targeting multi-scale and high-resolution pansharpening:** existing resources [7, 32, 41] provide limited scale diversity and spatial resolution, falling short of real-world needs and constraining the development and fair assessment of advanced methods under high-resolution, cross-scale conditions.

To address these challenges, we introduce PanScale-Datasets, the first cross-scale remote sensing image fusion dataset specifically designed for pansharpening in multi-resolution and high-resolution scenarios. The dataset comprises satellite imagery from three types of remote sensing platforms, with native spatial resolutions ranging from 0.5 meters to 15 meters, thereby covering a broad spectrum of

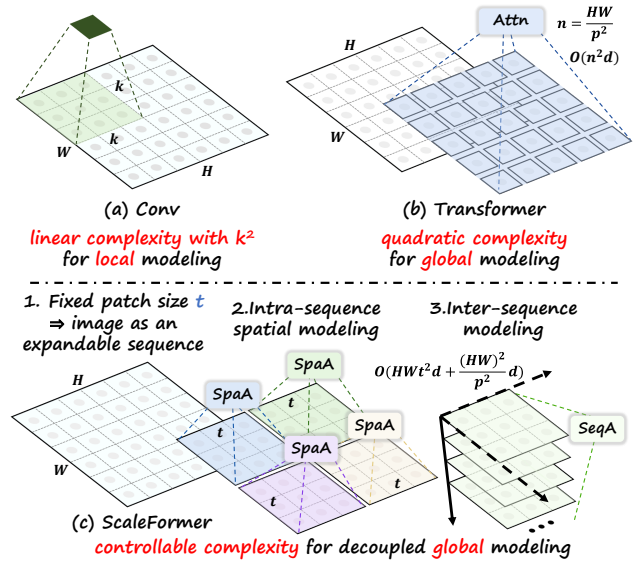


Figure 2. Comparison of convolution, Transformer, and the proposed ScaleFormer. (a) Convolution: linear in image size but with a limited receptive field on high-resolution inputs; enlarging kernels helps but adds quadratic cost in kernel size. (b) Transformer: uniform patchification enables global context, yet self-attention scales quadratically with patch count, driving computation up on large images. (c) ScaleFormer (ours): introduces a sequence axis, factorizing global modeling into fixed-size spatial processing plus a scalable sequence dimension, yielding controllable complexity and mitigating scale-induced distribution shifts for robust performance across resolutions.

real-world sensing conditions. To simulate practical multi-scale processing demands, we construct a series of reduced-resolution and full-resolution test sets, ranging in size from 200×200 to 2000×2000 pixels, enabling rigorous evaluation under diverse input resolutions and spatial scales. In conjunction with the dataset, we propose a comprehensive evaluation suite, PanScale-Bench, which supports standardized and fair benchmarking across different methods. It integrates a variety of reference-based and no-reference metrics to comprehensively assess fusion quality at varying scales, offering a unified platform for performance comparison and analysis within the community.

Building upon this, we introduce ScaleFormer, a framework designed for robust remote-sensing image fusion across diverse scales and resolutions. As outlined in Fig. 2, the core idea is to reinterpret resolution changes as sequence-length changes: local patches at a fixed spatial size serve as statistically stable tokens, and only the sequence length grows linearly with image size. Concretely, we propose Scale-Aware Patchify (SAP), which employs bucketed window sampling during training to expose the model to multiple effective sequence lengths, thereby stabilizing per-token mean and variance and narrowing the training-inference distribution gap.

We further adopt decoupled intra-spatial and inter-sequence modeling, and incorporate RoPE [37] to enhance extrapolation to unseen sequence lengths corresponding to larger resolutions. This reformulation markedly reduces VRAM and GFLOPs at large scales and avoids the tiling artifacts common in blockwise inference. Extensive experiments on the PanScale dataset demonstrate that ScaleFormer achieves accurate and efficient fusion over a wide range of scales and resolutions, confirming its effectiveness and advantage for multi-scale pansharpening.

Our contributions can be summarized as follows:

- We present PanScale, the first cross-scale pansharpening dataset, together with PanScale-Bench, a comprehensive evaluation benchmark. This standardized platform enables systematic testing and assessment of pansharpening methods in diverse multi-scale and high-resolution scenarios encountered in real-world applications.
- We propose ScaleFormer, a framework designed for robust multi-scale pansharpening. It reframes the problem of generalizing to unseen image resolutions as generalizing to unseen sequence lengths. ScaleFormer achieves this by decoupling the modeling of fine-grained spatial structures within image patches and the scale-adaptive sequential dependencies between these patches, leading to stable performance across various input resolutions.
- We incorporate bucket training strategy and rotary positional encoding to promote better generalization to unseen scales. These techniques encourage the model to adapt to varying resolutions beyond those seen during training.
- Extensive experiments across multiple datasets within the PanScale demonstrate that our method achieves accurate and efficient fusion at multiple scales and maintains high performance even when processing ultra-high-resolution inputs, highlighting its strong generalization ability and practical applicability in real-world multi-scale fusion.

2. Related Work

Please refer to the Appendix 8.

3. Proposed Datasets and Benchmark

3.1. Data Collection and Preprocessing

To construct the PanScale Datasets, we leveraged the capabilities of Google Earth Engine (GEE) [13] to systematically acquire and preprocess multi-source remote sensing data. The overall data preparation pipeline and detailed process are in the Appendix 9.1.

3.2. Dataset composition and benchmark design

Most existing pansharpening methods are evaluated on relatively small-scale datasets with fixed resolutions, which limits their applicability to real-world scenarios involving high-resolution satellite imagery. To comprehensively assess the

generalization ability of fusion methods on multi-scale, high-resolution inputs, we designed the PanScale dataset, which consists of three sub-datasets. Each sub-dataset includes a training set, multi-scale reduced-resolution test sets, and multi-scale full-resolution test sets. The detailed configurations of these datasets are summarized in Fig. 3. A more comprehensive description can be found in Appendix 9.2. Furthermore, the benchmark design is provided in Appendix 9.3.

Table 1 presents a comparison between the PanScale dataset and several widely used pansharpening datasets, focusing on the following aspects: data type, whether the data is real, the inclusion of a training set, and support for Multi-Resolution Testing (MRT) and Large Scale Testing (LST). It is evident that our dataset is unique in its simultaneous emphasis on both training data and large-scale testing, and is the only one that includes cross-scale evaluation.

Table 1. Comparison between the PanScale dataset and widely used pansharpening datasets, focusing on data type, whether the data is real, the inclusion of a training set, and support for Multi-Resolution Testing (MRT) and Large Scale Testing (LST).

Datasets	Type	Real data	Train	MRT	LST
PanCollection[7]	RR and FR	✓	✓	✗	✗
NBU[32]	FR	✓	✓	✗	✗
PAirMax[41]	RR and FR	✓	✗	✗	✓
PanScale	RR and FR	✓	✓	✓	✓

4. Proposed Methods

4.1. Overview

Fig. 4 illustrates the overall architecture of the proposed ScaleFormer, which is composed of three primary components: (1) the Scale-Aware Patchify module that incorporates a bucket-based training strategy to promote scale diversity and robustness; (2) Single-Transformer modules consisting of the Spatial-Transformer and Sequence-Transformer, each dedicated to modeling spatial and sequential dependencies independently; and (3) Cross-Transformer modules that include the Spatial-Cross Transformer and Sequence-Cross Transformer, which facilitate cross-modal interactions through cross-attention mechanisms along spatial and sequential dimensions, respectively. Given an input panchromatic image $\mathbf{P} \in \mathbb{R}^{H \times W \times 1}$ and a corresponding low-resolution multi-spectral (LRMS) image $\mathbf{L}_{in} \in \mathbb{R}^{(H/r) \times (W/r) \times C}$, where r denotes the upsampling ratio between the two modalities, we first apply bicubic interpolation to \mathbf{L}_{in} to obtain an upsampled multi-spectral image $\mathbf{L} \in \mathbb{R}^{H \times W \times C}$ that matches the spatial dimensions of the PAN image. The Scale-Aware Patchify module performs randomized sliding window sampling at various patch sizes

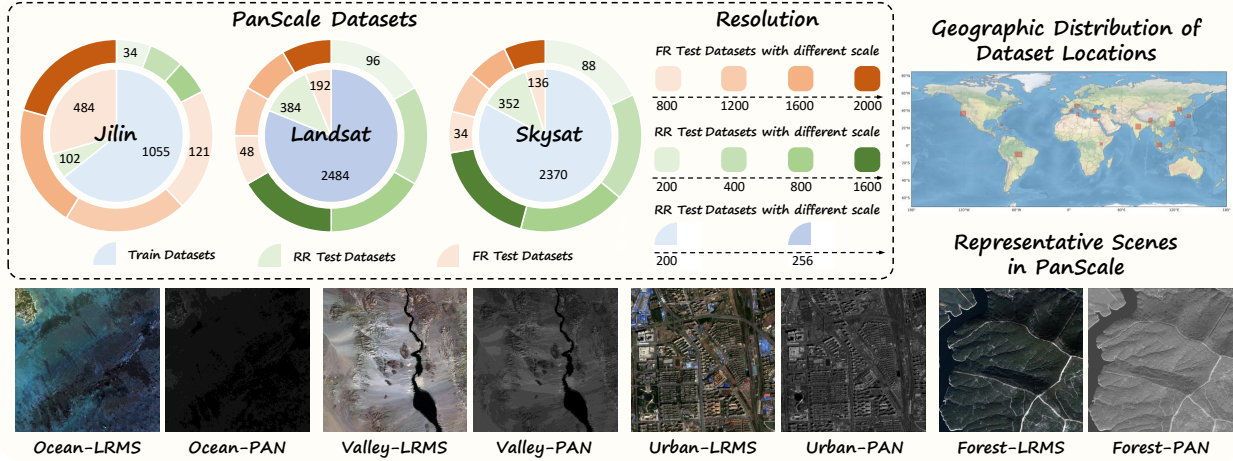


Figure 3. PanScale dataset: composition and distribution, resolution range, geographic sampling locations, and representative scene visualizations.

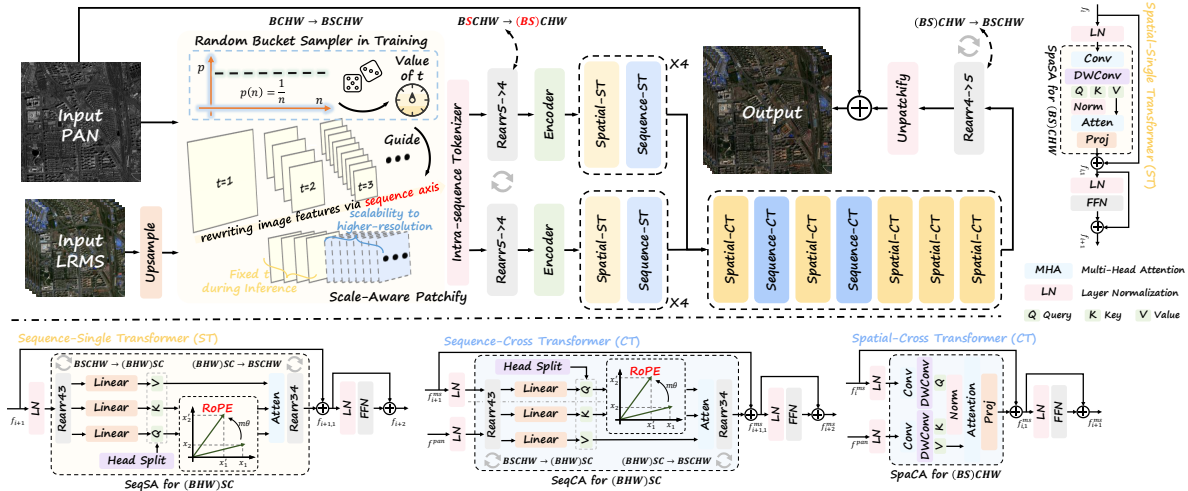


Figure 4. The overall architecture of ScaleFormer, which primarily consists of three key components: the Scale-Aware Patchify module implementing the bucket sampling strategy, the Single Transformer Modules for intra-modal feature modeling, and the Cross Transformer Modules for inter-modal feature interaction and fusion.

to enable multi-scale representation learning. The extracted patches are then concatenated along a newly introduced sequence dimension, effectively converting spatially aligned inputs into a sequence of multi-scale tokens suitable for subsequent transformer-based modeling:

$$\mathbf{P}_{5d}, \mathbf{L}_{5d} = \text{SAP}(\mathbf{P}), \text{SAP}(\mathbf{L}) \quad (1)$$

where SAP represents the operation of Scale-Aware Patchify, $\mathbf{P}_{5d} \in \mathbb{R}^{B \times T \times C \times h \times w}$, $\mathbf{L}_{5d} \in \mathbb{R}^{B \times T \times C \times h \times w}$, $h = H/T$, $w = W/T$. To facilitate subsequent processing, we reshape \mathbf{P}_{5d} and \mathbf{L}_{5d} by merging the batch and sequence dimensions. These are then passed through a lightweight feature encoder to extract deep feature

representations for each modality, denoted as \mathbf{f}_{4d}^{pan} and \mathbf{f}_{4d}^{ms} :

$$\mathbf{f}_{4d}^{pan}, \mathbf{f}_{4d}^{ms} = \text{Enc}(R_{54}(\mathbf{P}_{5d})), \text{Enc}(R_{54}(\mathbf{L}_{5d})) \quad (2)$$

Here, R_{54} denotes the tensor rearrangement operation that transforms a 5D representation into a 4D format. Following this, we employ a cascaded structure consisting of a Spatial Transformer and a Sequence Transformer to perform hierarchical feature extraction across both the spatial and the newly introduced scale dimensions within each modality.

To enhance cross-modal interaction and facilitate more effective feature fusion, we further introduce Spatial-Cross Transformer and Sequence-Cross Transformer modules. These modules enable bidirectional information exchange between the panchromatic and multi-spectral features along

spatial and scale dimensions, respectively, yielding a fused representation denoted as \mathbf{F}_{4d}^{fus} . To accurately reconstruct the high-resolution multi-spectral output, we apply an inverse rearrangement operation to decompose the sequence dimension of \mathbf{F}_{4d}^{fus} , followed by a patch reassembly process. This final step produces the desired high-resolution multi-spectral image, denoted as \mathbf{H}_{out} .

4.2. Scale-Aware Patchify

To mitigate the distribution shift that arises as input resolution increases, we introduce a Scale-Aware Patchify (SAP) module that equips the model with explicit awareness of spatial scale. SAP rewrites local image evidence into an additional sequence axis, enabling subsequent components to perform spatial modeling within patches while conducting inter-sequence modeling along the sequence. This decoupling preserves spatial granularity inside each window and delegates scale variation to the sequence length, improving robustness when the input size changes. Inspired by recent progress in multi-resolution training for video generation [5, 35, 54], we further adopt bucketed sampling to expose the network to unseen sequence lengths during training. Concretely, given co-registered panchromatic (PAN) and multispectral (MS) inputs, we randomly sample a bucket index t that determines a pre-defined window size $w(t)$. A Patch-to-Sequence Tokenizer then partitions the inputs using $w(t)$, producing a token sequence whose length encodes the effective scale. This procedure increases the model’s coverage of resolution variability, narrowing the gap between the training distribution and the test-time operating points. In inference, the system deterministically uses a fixed window size (probability 100%), so that higher spatial resolutions are handled simply by lengthening the sequence along the scale axis while keeping per-token statistics stable. In effect, SAP prevents the mean and variance drift that typically accompanies scale changes and allows explicit and independent modeling of spatial and scale correlations. This design yields strong generalization across diverse and previously unseen input resolutions, aligning with the goals of cross-scale pan-sharpening in ScaleFormer and the evaluation protocols of the PanScale Benchmark.

4.3. Single Transformer Modules

Following the Scale-Aware Patchify, the input images are transformed into fixed-size spatial patches while introducing an additional sequence dimension that encodes scale-aware structural information. To facilitate effective learning across spatial and sequential representations, we introduce a Single-Transformer module consisting of a Spatial Transformer and a Sequence Transformer. These modules are specialized to independently capture dependencies within the spatial and sequential domains, respectively. The Spatial Transformer focuses on modeling local and global spatial relationships

within each patch, enabling the network to extract rich spatial features. In parallel, the Sequence Transformer operates along the newly introduced sequence dimension, learning cross-patch correlations and capturing scale-aware contextual dependencies. This separation of concerns allows the model to decouple spatial encoding from scale modeling, thus improving both representation capacity and scalability across varying input resolutions. Specifically, given an input feature map $\mathbf{f}_{i,1}$, the Single-Transformer module processes it sequentially along the spatial and sequence dimensions. This procedure can be formally described as follows:

$$\mathbf{f}_{i,1} = \mathbf{f}_i + SA_{spa}(LN(\mathbf{f}_i)) \quad (3)$$

$$\mathbf{f}_{i+1} = \mathbf{f}_{i,1} + FFN(LN(\mathbf{f}_{i,1})) \quad (4)$$

$$\mathbf{f}_{i+1,1} = \mathbf{f}_{i+1} + SA_{seq}(LN(\mathbf{f}_{i+1})) \quad (5)$$

$$\mathbf{f}_{i+2} = \mathbf{f}_{i+1,1} + FFN(LN(\mathbf{f}_{i+1,1})) \quad (6)$$

where SA_{spa} denotes the self-attention operation applied along the spatial dimensions, and LN represents the Layer Normalization. Subsequently, SA_{seq} applies self-attention along the sequence dimension. To facilitate this, we perform a rearrangement operation that merges the batch and spatial dimensions into a single axis. Additionally, we incorporate Rotary Position Embedding (RoPE) [37] into the mapped queries and keys, which significantly enhances the model’s ability for scale extrapolation by encoding continuous relative positional information.

4.4. Cross Transformer Modules

Similarly, the Cross Transformer module comprises a Spatial Cross Transformer and a Sequence Cross Transformer. Specifically, given the input feature maps \mathbf{f}_i^{ms} and \mathbf{f}^{pan} , the stacked Spatial-Cross Transformer and Sequence-Cross Transformer perform a series of cross-attention operations to facilitate effective interaction and information fusion between the multi-spectral and panchromatic features. The computation can be expressed as:

$$\mathbf{f}_{i,1}^{ms} = \mathbf{f}_i^{ms} + CA_{spa}(LN(\mathbf{f}_i^{ms}), LN(\mathbf{f}^{pan})) \quad (7)$$

$$\mathbf{f}_{i+1}^{ms} = \mathbf{f}_{i,1}^{ms} + FFN(LN(\mathbf{f}_{i,1}^{ms})) \quad (8)$$

$$\mathbf{f}_{i+1,1}^{ms} = \mathbf{f}_{i+1}^{ms} + CA_{seq}(LN(\mathbf{f}_{i+1}^{ms}), LN(\mathbf{f}^{pan})) \quad (9)$$

$$\mathbf{f}_{i+2,1}^{ms} = \mathbf{f}_{i+1,1}^{ms} + FFN(LN(\mathbf{f}_{i+1,1}^{ms})) \quad (10)$$

Here, LN denotes Layer Normalization. CA_{spa} refers to the cross-attention mechanism along the spatial dimensions, while CA_{seq} operates on the sequence dimension. Similar to the single-modality attention, we apply a rearrangement operation during CA_{seq} to merge the batch and spatial dimensions into a single axis. RoPE is also injected into the projected queries and keys, which enhances the model’s capacity for generalizing across scales by encoding relative positional information.

Table 2. Quantitative Results on PanScale Datasets. The best results are highlighted in **bold**. The second-best results are highlighted in underline. \uparrow indicates that the larger the value, the better the performance, and \downarrow indicates that the smaller the value, the better the performance. ARConv uses tiled inference due to OOM, and other methods are evaluated with train–inference scale misalignment.

Method	Jilin-Ave				Landsat-Ave				Skysat-Ave			
	PSNR \uparrow	SSIM \uparrow	ERGAS \downarrow	Q \uparrow	PSNR \uparrow	SSIM \uparrow	ERGAS \downarrow	Q \uparrow	PSNR \uparrow	SSIM \uparrow	ERGAS \downarrow	Q \uparrow
GS	25.4386	0.7055	5.6091	0.5849	35.0781	0.8952	4.5954	0.5873	39.0558	0.9317	2.3673	0.6371
IHS	25.5950	0.7023	5.8071	0.5803	35.8777	0.8915	4.3234	0.5554	39.5900	0.9304	2.1756	0.6271
GFPCA	25.6134	0.7185	5.0460	0.4509	36.2597	0.8963	3.6041	0.4747	37.6663	0.9280	2.4973	0.4773
MSDCNN	36.5711	0.9574	1.4965	0.9092	38.8173	0.9592	2.6570	0.6737	42.5298	0.9696	2.5983	0.7261
SFINet	36.2845	0.9523	1.6129	0.8958	38.8276	0.9567	2.8075	0.6739	41.7457	0.9518	2.9933	0.6950
MSDDN	36.9407	0.9646	1.4326	0.9195	37.6899	0.9346	2.9023	0.6421	41.0392	0.9456	2.8546	0.6949
PanFlowNet	36.3326	0.9566	1.5554	0.9067	38.2158	0.9433	3.2700	0.6669	41.0219	0.9530	2.9228	0.6728
HFIN	38.0009	<u>0.9698</u>	1.2754	<u>0.9284</u>	40.2110	<u>0.9666</u>	<u>2.3230</u>	<u>0.7216</u>	<u>43.9592</u>	0.9658	2.2738	<u>0.7707</u>
Pan-mamba	35.5514	0.9480	1.6963	0.8966	36.7272	0.9206	3.2483	0.6437	41.3851	0.9493	2.7667	0.7129
ARConv	<u>38.2340</u>	0.9697	<u>1.2462</u>	0.9291	39.6646	0.9638	2.4441	0.6866	43.4037	<u>0.9797</u>	<u>2.0629</u>	0.7564
Ours	39.2932	0.9761	1.0991	0.9385	41.0360	0.9711	2.1354	0.7395	44.6546	0.9827	1.7293	0.7835

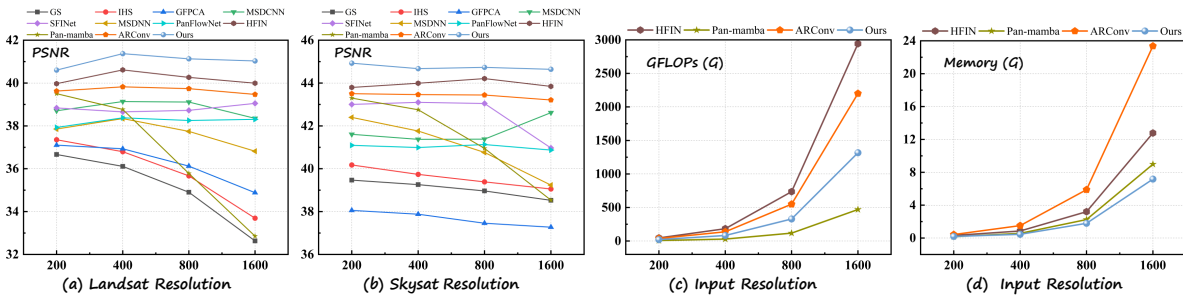


Figure 5. Comparison results across increasing resolution scales. The four subplots respectively depict: (a) PSNR score on the Landsat dataset, (b) PSNR score on the Skysat dataset, (c) model computational complexity (measured in GFLOPs) as a function of input resolution, and (d) Memory variation concerning input resolution.

4.5. Loss Function

Following common practices in the field [3, 24, 25, 38], we employ the L1 norm as the loss function during training, which measures the pixel-wise discrepancy between the output image \mathbf{H}_{out} and the ground truth \mathbf{G} . The loss can be formally defined as:

$$\mathbf{L} = \|\mathbf{H}_{out} - \mathbf{G}\|_1 \quad (11)$$

5. Experiments

5.1. Implementation Details

In the comparative experiments, we selected a range of representative traditional methods as well as state-of-the-art deep learning techniques, including GS [22], IHS [15], GFPCA [26], MSDCNN [50], SFINet [57], MSDDN [16], PanFlowNet [49], HFIN [38], Pan-mamba [17], and ARConv [44]. These methods encompass a wide spectrum of approaches, ranging from classical image fusion techniques to the most recent deep learning-based models, thereby pro-

viding a comprehensive comparison for evaluating the performance of our proposed method. To ensure consistency and fairness, all methods are trained separately on the three training sets of the PanScale-Datasets and assessed on the corresponding RR and FR multi-resolution test sets. Additionally, the evaluation metrics are derived from the PanScale-Bench, providing a comprehensive and standardized basis for performance assessment. Our experimental framework is implemented using PyTorch, with all training performed on an NVIDIA 3090 GPU. The model is configured with 32 feature channels. We employed a cosine-annealed decay strategy for the learning rate, with an initial rate of 5×10^{-4} that gradually decays to 5×10^{-8} over 500 epochs. We optimize the model using the Adam optimizer [21], with gradient clipping set to 4.

5.2. Comparison with the SOTA Methods

Quantitative Comparison As shown in the comparative analysis in Table 2, we evaluated our proposed method against several state-of-the-art pansharpening approaches.

Table 3. Evaluation of our method on real-world full-resolution scenes from three datasets.

Method	Full-Jilin-Ave			Full-Landsat-Ave			Full-Skysat-Ave		
	$D_\lambda \downarrow$	$D_S \downarrow$	QNR \uparrow	$D_\lambda \downarrow$	$D_S \downarrow$	QNR \uparrow	$D_\lambda \downarrow$	$D_S \downarrow$	QNR \uparrow
GS	0.0812	0.2021	0.7338	0.0568	0.1110	0.8393	0.0623	0.1112	0.8347
IHS	0.0971	0.2124	0.7116	0.0961	0.1233	0.7936	0.0974	0.1318	0.7852
GFPCA	0.0424	0.0985	0.8633	0.0649	0.0539	0.8850	0.0433	0.0624	0.8976
MSDCNN	0.0477	0.0420	0.9126	0.0488	0.0326	0.9214	0.0419	0.0222	0.9403
SFINet	0.0538	0.0439	0.9050	0.0425	0.0342	0.9255	0.1346	0.0334	0.8379
MSDDN	<u>0.0415</u>	0.0521	0.9097	0.0336	0.0236	0.9442	0.0412	0.0363	0.9264
PanFlowNet	0.0459	0.0382	<u>0.9155</u>	0.0482	0.0384	0.9159	0.0777	0.0332	0.8927
HFIN	0.0424	0.0471	0.9129	<u>0.0240</u>	0.0197	<u>0.9562</u>	0.0591	0.0590	0.8865
Pan-mamba	0.0465	0.0426	0.9132	0.0309	0.0736	0.8979	0.0533	0.0311	0.9182
ARConv	0.0417	0.0629	0.8980	0.0257	<u>0.0201</u>	0.9550	0.0387	0.0409	0.9225
Ours	0.0409	<u>0.0418</u>	0.9156	0.0234	0.0228	0.9569	<u>0.0405</u>	<u>0.0269</u>	0.9408

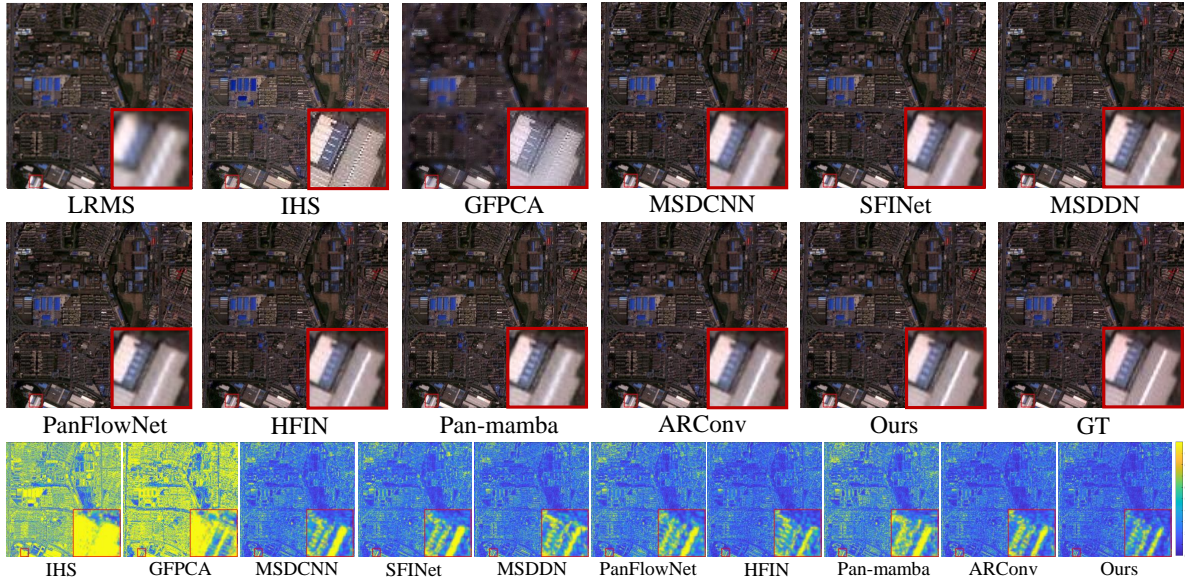


Figure 6. Comparative visual experiments of several methods on Jilin datasets.

Table 4. Evaluation of parameter count and GFLOPs.

Methods	MSDCNN	SFINet	MSDDN	PanFlowNet	HFIN	Pan-mamba	ARConv	Ours
Params(M)	0.2390	0.0484	0.3649	0.0873	1.9836	0.1828	4.4147	0.5151
GFLOPs(G)	9.5488	1.8785	7.6938	13.9469	46.2067	7.3459	38.3152	20.5679

Table 5. Ablation study of our method on the Landsat test set. The best are highlighted in **bold**, and the second are underlined.

Ablation	Landsat-200		Landsat-400		Landsat-800		Landsat-1600	
	PSNR \uparrow	SSIM \uparrow						
w/o RoPE	40.4625	0.9682	40.9542	0.9704	<u>40.7619</u>	0.9699	40.6924	0.9701
SeqT -> SpaT	40.9061	0.9700	<u>41.2964</u>	0.9724	<u>40.7206</u>	<u>0.9714</u>	40.5065	0.9716
w/o SAP	40.5279	0.9660	40.9325	0.9692	40.6186	0.9688	40.3895	0.9689
Baseline	<u>40.6063</u>	<u>0.9677</u>	41.3715	0.9725	41.1326	0.9719	41.0335	0.9722

For brevity, the reported results represent the average performance across multiple resolution settings within each dataset; the complete results for individual resolutions are provided in the appendix 10.2. Our method consistently and significantly outperforms all competing methods across all evaluation metrics, demonstrating its strong fusion quality and robustness. To further assess the adaptability of our approach to varying input resolutions, we visualize the PSNR scores of different methods on the Landsat and Skysat datasets across a range of resolution scales, as illustrated in Fig. 5(a) and (b). While our method maintains stable performance as the input resolution increases, the other methods exhibit noticeable performance degradation to varying degrees. These results highlight the superior scalability and generalization ability of ScaleFormer in handling diverse and high-resolution remote sensing data.

To validate the proposed ScaleFormer’s real-world performance, we conducted experiments on three full-resolution datasets from the PanScale benchmark, each containing four test sets at varying spatial scales. Due to the lack of ground truth in these real-world scenarios, we employed three no-reference metrics from PanScale-Bench to assess model performance. For conciseness, the main text reports the average results across different resolutions within each dataset, while detailed per-scale results are provided in the appendix 10.2. As shown in Table 3, ScaleFormer consistently achieves competitive performance across all evaluation metrics, demonstrating its strong generalization ability and robustness in complex, real-world multi-resolution fusion tasks.

To evaluate the efficiency of the proposed approach, we compare the model’s parameter count and computational complexity with those of several baseline methods. All experiments in Table 4 were conducted with input resolutions set to 200×200 . ScaleFormer demonstrates a comparable parameter count to Pan-mamba [17], which is less than one-fourth of the state-of-the-art methods, HFIN [38] and ARConv [44]. This significant reduction in parameter count highlights the efficiency of ScaleFormer relative to these methods. Furthermore, the proposed method exhibits a clear advantage in computational complexity over these two advanced methods, underscoring its competitiveness in resource usage and overall efficiency. As illustrated in Fig. 5(c) and (d), this advantage becomes even more prominent as the input resolution increases, with ScaleFormer maintaining significantly lower GFLOPs and memory consumption compared to SOTA methods. This showcases that ScaleFormer offers a compelling balance between performance and computational cost, making it an efficient solution for large-scale and multi-resolution data.

Qualitative Comparison The qualitative comparison results are presented in Fig. 6, with more visualizations in the appendix 10.1. We visualize representative samples at the largest resolution scale from each dataset, and further mag-

nify selected regions to facilitate detailed comparison. The final row of each qualitative figure shows the mean squared error (MSE) maps between the pansharpened and reference images, where brighter areas indicate larger discrepancies. As shown in these figures, the proposed method demonstrates clear advantages in preserving fine spatial details and spectral fidelity, yielding sharper textures and more visually coherent results.

5.3. Ablation Studies

To validate the effectiveness of the proposed method, we conduct a series of ablation studies on the Landsat dataset, focusing on key components of the ScaleFormer architecture. The corresponding PSNR and SSIM results are summarized in Table 5. Specifically, we examine the impact of the following modifications: (1) removing the RoPE from the Sequence Transformer (including the single and the cross); (2) replacing the Sequence Transformer with their corresponding Spatial Transformer counterparts, thereby discarding the scale dimension modeling; and (3) removing the SAP by fixing the training window size to a single static setting, aligned with the configuration used during inference.

As shown in the results, all ablation variants exhibit a clear and consistent decline in performance as the test resolution increases, compared to the full model. This degradation highlights the limitations of these configurations in generalizing across scales. In particular, the absence of RoPE hinders the model’s capacity to encode relative positional dependencies effectively across varying resolutions. Replacing sequence attention with purely spatial attention deprives the model of its ability to capture inter-patch relationships across sequence-like structures, which are critical for generalizing to unseen scales. Additionally, removing the SAP module prevents the model from learning a diverse and adaptive representation during training, making it less robust to scale shifts encountered at inference time. These findings highlight that the proposed component can enhance scale-awareness and extrapolate beyond the training distribution.

6. Conclusion

We propose ScaleFormer, a framework that decouples spatial information from scale-specific features and models them independently. By incorporating a bucketed training strategy and Rotary Position Embeddings (RoPE), ScaleFormer markedly improves scale extrapolation. To enable fair and comprehensive evaluation, we introduce PanScale, addressing the lack of multi-scale inference in existing datasets; to our knowledge, it is the first pansharpening dataset to jointly cover multi-scale and multi-resolution characteristics, accompanied by a tailored evaluation suite, PanScale-Bench. Extensive experiments across PanScale demonstrate that ScaleFormer surpasses state-of-the-art methods in both fusion quality and computational efficiency.

7. Acknowledgments

We thank Lingting Zhu for the discussions on the method.

References

- [1] Luciano Alparone, Bruno Aiazzi, Stefano Baronti, Andrea Garzelli, Filippo Nencini, and Massimo Selva. Multispectral and panchromatic data fusion assessment without reference. *Photogrammetric Engineering & Remote Sensing*, 74(2):193–200, 2008. 2
- [2] Lucas Beyer, Pavel Izmailov, Alexander Kolesnikov, Mathilde Caron, Simon Kornblith, Xiaohua Zhai, Matthias Minderer, Michael Tschannen, Ibrahim Alabdulmohsin, and Filip Pavetic. Flexivit: One model for all patch sizes. In *Proceedings of the IEEE/CVF Conference on Computer Vision and Pattern Recognition*, pages 14496–14506, 2023. 1
- [3] Ke Cao, Xuanhua He, Tao Hu, Chengjun Xie, Jie Zhang, Man Zhou, and Danfeng Hong. Shuffle mamba: State space models with random shuffle for multi-modal image fusion. *arXiv preprint arXiv:2409.01728*, 2024. 6
- [4] Zihan Cao, Xiao Wu, Liang-Jian Deng, and Yu Zhong. A novel state space model with local enhancement and state sharing for image fusion. In *Proceedings of the 32nd ACM International Conference on Multimedia*, pages 1235–1244, 2024. 1
- [5] Junsong Chen, Jincheng Yu, Chongjian Ge, Lewei Yao, Enze Xie, Yue Wu, Zhongdao Wang, James Kwok, Ping Luo, Huchuan Lu, et al. Pixart- α : Fast training of diffusion transformer for photorealistic text-to-image synthesis. *arXiv preprint arXiv:2310.00426*, 2023. 5
- [6] Xiaojie Chu, Liangyu Chen, Chengpeng Chen, and Xin Lu. Improving image restoration by revisiting global information aggregation. In *European Conference on Computer Vision*, pages 53–71. Springer, 2022. 2
- [7] Liang-Jian Deng, Gemine Vivone, Mercedes E Paoletti, Giuseppe Scarpa, Jiang He, Yongjun Zhang, Jocelyn Chanussot, and Antonio Plaza. Machine learning in pansharpening: A benchmark, from shallow to deep networks. *IEEE Geoscience and Remote Sensing Magazine*, 10(3):279–315, 2022. 2, 3
- [8] Qihang Fan, Quanzeng You, Xiaotian Han, Yongfei Liu, Yunzhe Tao, Huaibo Huang, Ran He, and Hongxia Yang. Vitar: Vision transformer with any resolution. *arXiv preprint arXiv:2403.18361*, 2024. 1
- [9] Jiabin Fang, Ke Cao, Xuanhua He, Jie Zhang, Man Zhou, and Liu Liu. Pandit: A few-step diffusion transformer for high-fidelity and efficient pansharpening. *IEEE Transactions on Geoscience and Remote Sensing*, 63:1–13, 2025. 1
- [10] Dominique Fasbender, Julien Radoux, and Patrick Bogaert. Bayesian data fusion for adaptable image pansharpening. *IEEE Transactions on Geoscience and Remote Sensing*, 46(6):1847–1857, 2008. 1
- [11] Morteza Ghahremani and Hassan Ghassemian. A compressed-sensing-based pan-sharpening method for spectral distortion reduction. *IEEE Transactions on Geoscience and Remote Sensing*, 54(4):2194–2206, 2015. 1
- [12] Alan R Gillespie, Anne B Kahle, and Richard E Walker. Color enhancement of highly correlated images. ii. channel ratio and “chromaticity” transformation techniques. *Remote Sensing of Environment*, 22(3):343–365, 1987. 1
- [13] Noel Gorelick, Matt Hancher, Mike Dixon, Simon Ilyushchenko, David Thau, and Rebecca Moore. Google earth engine: Planetary-scale geospatial analysis for everyone. *Remote sensing of Environment*, 202:18–27, 2017. 3
- [14] R Haydn. Application of the ihs color transform to the processing of multisensor data and image enhancement. In *Proc. of the International Symposium on Remote Sensing of Arid and Semi-Arid Lands, Cairo, Egypt, 1982*, 1982. 1
- [15] R. Haydn, G. W. Dalke, J. Henkel, and J. E. Bare. Application of the ihs color transform to the processing of multisensor data and image enhancement. *National Academy of Sciences of the United States of America*, 79(13):571–577, 1982. 6
- [16] Xuanhua He, Keyu Yan, Jie Zhang, Rui Li, Chengjun Xie, Man Zhou, and Danfeng Hong. Multi-scale dual-domain guidance network for pan-sharpening. *IEEE Transactions on Geoscience and Remote Sensing*, 2023. 6, 1
- [17] Xuanhua He, Ke Cao, Jie Zhang, Keyu Yan, Yingying Wang, Rui Li, Chengjun Xie, Danfeng Hong, and Man Zhou. Panmamba: Effective pan-sharpening with state space model. *Information Fusion*, 115:102779, 2025. 6, 8
- [18] Quan Huynh-Thu and Mohammed Ghanbari. Scope of validity of psnr in image/video quality assessment. *Electronics letters*, 44(13):800–801, 2008. 2
- [19] Harry H Kelejian and Dennis P Robinson. Spatial correlation: a suggested alternative to the autoregressive model. In *New directions in spatial econometrics*, pages 75–95. Springer, 1995. 2
- [20] Muhammad Murtaza Khan, Luciano Alparone, and Jocelyn Chanussot. Pansharpening quality assessment using the modulation transfer functions of instruments. *IEEE transactions on geoscience and remote sensing*, 47(11):3880–3891, 2009. 2
- [21] Diederik P Kingma and Jimmy Ba. Adam: A method for stochastic optimization. *arXiv preprint arXiv:1412.6980*, 2014. 6
- [22] C.A. Laben and B.V. Brower. Process for enhancing the spatial resolution of multispectral imagery using pan-sharpening. *US Patent 6011875A*, 2000. 6, 1
- [23] Shutao Li and Bin Yang. A new pan-sharpening method using a compressed sensing technique. *IEEE Transactions on Geoscience and Remote Sensing*, 49(2):738–746, 2010. 1
- [24] Xueheng Li, Xuanhua He, Ke Cao, Jie Zhang, Chengjun Xie, Man Zhou, Danfeng Hong, and Bo Huang. Exploring text-guided information fusion through chain-of-reasoning for pan-sharpening. *IEEE Transactions on Geoscience and Remote Sensing*, 2025. 6
- [25] Xueheng Li, Tao Hu, Ke Cao, Jie Zhang, Chengjun Xie, Man Zhou, and Danfeng Hong. Pan-sharpening via causal-aware feature distribution calibration. *IEEE Transactions on Geoscience and Remote Sensing*, 2025. 6
- [26] W. Liao, H. Xin, F. V. Coillie, G. Thoonen, and W. Philips. Two-stage fusion of thermal hyperspectral and visible rgb image by pca and guided filter. In *Workshop on Hyperspectral*

Image and Signal Processing: Evolution in Remote Sensing, 2017. 6

- [27] Yunlong Lin, Zhenqi Fu, Ge Meng, Yingying Wang, Yuhang Dong, Linyu Fan, Hedeng Yu, and Xinghao Ding. Domain-irrelevant feature learning for generalizable pan-sharpening. In *Proceedings of the 31st ACM International Conference on Multimedia*, pages 3287–3296, 2023. 1
- [28] J. G. Liu. Smoothing filter-based intensity modulation: A spectral preserve image fusion technique for improving spatial details. *International Journal of Remote Sensing*, 21(18): 3461–3472, 2000. 1
- [29] Wenzhuo Liu, Fei Zhu, Shijie Ma, and Cheng-Lin Liu. Mspe: Multi-scale patch embedding prompts vision transformers to any resolution. *arXiv preprint arXiv:2405.18240*, 2024. 1
- [30] Stephane G Mallat. A theory for multiresolution signal decomposition: the wavelet representation. *IEEE transactions on pattern analysis and machine intelligence*, 11(7):674–693, 1989. 1
- [31] Giuseppe Masi, Davide Cozzolino, Luisa Verdoliva, and Giuseppe Scarpa. Pansharpening by convolutional neural networks. *Remote Sensing*, 8(7), 2016. 1
- [32] Xiangchao Meng, Yiming Xiong, Feng Shao, Huanfeng Shen, Weiwei Sun, Gang Yang, Qiangqiang Yuan, Randi Fu, and Hongyan Zhang. A large-scale benchmark data set for evaluating pansharpening performance: Overview and implementation. *IEEE Geoscience and Remote Sensing Magazine*, 9(1):18–52, 2020. 2, 3
- [33] Frosti Palsson, Johannes R Sveinsson, and Magnus O Ulfarson. A new pansharpening algorithm based on total variation. *IEEE Geoscience and Remote Sensing Letters*, 11(1):318–322, 2013. 1
- [34] Siran Peng, Xiangyu Zhu, Haoyu Deng, Liang-Jian Deng, and Zhen Lei. Fusionmamba: Efficient remote sensing image fusion with state space model. *IEEE Transactions on Geoscience and Remote Sensing*, 62:1–16, 2024. 1
- [35] Dustin Podell, Zion English, Kyle Lacey, Andreas Blattmann, Tim Dockhorn, Jonas Müller, Joe Penna, and Robin Rombach. Sdxl: Improving latent diffusion models for high-resolution image synthesis. *arXiv preprint arXiv:2307.01952*, 2023. 5
- [36] Robert A Schowengerdt. Reconstruction of multispatial, multispectral image data using spatial frequency content. *Photogrammetric Engineering and Remote Sensing*, 46(10):1325–1334, 1980. 1
- [37] Jianlin Su, Murtadha Ahmed, Yu Lu, Shengfeng Pan, Wen Bo, and Yunfeng Liu. Roformer: Enhanced transformer with rotary position embedding. *Neurocomputing*, 568:127063, 2024. 3, 5
- [38] Jiangtong Tan, Jie Huang, Naishan Zheng, Man Zhou, Keyu Yan, Danfeng Hong, and Feng Zhao. Revisiting spatial-frequency information integration from a hierarchical perspective for panchromatic and multi-spectral image fusion. In *Proceedings of the IEEE/CVF Conference on Computer Vision and Pattern Recognition*, pages 25922–25931, 2024. 2, 6, 8, 1
- [39] Rui Tian, Zuxuan Wu, Qi Dai, Han Hu, Yu Qiao, and Yu-Gang Jiang. Resformer: Scaling vits with multi-resolution training. In *Proceedings of the IEEE/CVF Conference on Computer Vision and Pattern Recognition*, pages 22721–22731, 2023. 1
- [40] Gemine Vivone, Luciano Alparone, Jocelyn Chanussot, Mauro Dalla Mura, Andrea Garzelli, Giorgio A Licciardi, Rocco Restaino, and Lucien Wald. A critical comparison among pansharpening algorithms. *IEEE Transactions on Geoscience and Remote Sensing*, 53(5):2565–2586, 2014. 1
- [41] Gemine Vivone, Mauro Dalla Mura, Andrea Garzelli, and Fabio Pacifici. A benchmarking protocol for pansharpening: Dataset, preprocessing, and quality assessment. *IEEE Journal of Selected Topics in Applied Earth Observations and Remote Sensing*, 14:6102–6118, 2021. 2, 3
- [42] Gemine Vivone, Mauro Dalla Mura, Andrea Garzelli, and Fabio Pacifici. A benchmarking protocol for pansharpening: Dataset, preprocessing, and quality assessment. *IEEE Journal of Selected Topics in Applied Earth Observations and Remote Sensing*, 14:6102–6118, 2021. 2
- [43] Lucien Wald. *Data fusion: definitions and architectures: fusion of images of different spatial resolutions*. Presses des MINES, 2002. 2
- [44] Xueyang Wang, Zhixin Zheng, Jiandong Shao, Yule Duan, and Liang-Jian Deng. Adaptive rectangular convolution for remote sensing pansharpening. *arXiv preprint arXiv:2503.00467*, 2025. 2, 6, 8, 1
- [45] Yingying Wang, Hui Zheng, Feifei Li, Yunlong Lin, Linyu Fan, Xuanhua He, Yue Huang, and Xinghao Ding. Towards generalizable pan-sharpening: Conditional flow-based learning guided by implicit high-frequency priors. *IEEE Transactions on Geoscience and Remote Sensing*, 2025. 1
- [46] Yingying Wang, Rongjin Zhuang, Hui Zheng, Xuanhua He, Ke Cao, Xiaotong Tu, and Xinghao Ding. Self-supervised multiplex consensus mamba for general image fusion. *arXiv preprint arXiv:2512.20921*, 2025. 1
- [47] Zhou Wang, Alan C Bovik, Hamid R Sheikh, and Eero P Simoncelli. Image quality assessment: from error visibility to structural similarity. *IEEE transactions on image processing*, 13(4):600–612, 2004. 2
- [48] Shuang Xu, Jianshe Zhang, Zixiang Zhao, Kai Sun, Junmin Liu, and Chunxia Zhang. Deep gradient projection networks for pan-sharpening. In *IEEE Conference on Computer Vision and Pattern Recognition*, pages 1366–1375, 2021. 1
- [49] Gang Yang, Xiangyong Cao, Wenzhe Xiao, Man Zhou, Aiping Liu, Xun Chen, and Deyu Meng. Panflownet: A flow-based deep network for pan-sharpening. In *Proceedings of the IEEE/CVF International Conference on Computer Vision*, pages 16857–16867, 2023. 6, 1
- [50] Q. Yuan, Y. Wei, X. Meng, H. Shen, and L. Zhang. A multi-scale and multidepth convolutional neural network for remote sensing imagery pan-sharpening. *IEEE Journal of Selected Topics in Applied Earth Observations and Remote Sensing*, 11(3):978–989, 2018. 6, 1
- [51] Roberta H Yuhas, Alexander FH Goetz, and Joe W Boardman. Discrimination among semi-arid landscape endmembers using the spectral angle mapper (sam) algorithm. In *JPL, Summaries of the Third Annual JPL Airborne Geoscience Workshop. Volume 1: AVIRIS Workshop*, 1992. 2
- [52] Jie Zhang, Ke Cao, Keyu Yan, Yunlong Lin, Xuanhua He, Yingying Wang, Rui Li, Chengjun Xie, Jun Zhang, and Man Zhou. Frequency decoupled domain-irrelevant feature learn-

- ing for pan-sharpening. *IEEE Transactions on Circuits and Systems for Video Technology*, 2024. 1
- [53] Jie Zhang, Xuanhua He, Keyu Yan, Ke Cao, Rui Li, Chengjun Xie, Man Zhou, and Danfeng Hong. Pan-sharpening with wavelet-enhanced high-frequency information. *IEEE Transactions on Geoscience and Remote Sensing*, 62:1–14, 2024. 2
- [54] Zangwei Zheng, Xiangyu Peng, Tianji Yang, Chenhui Shen, Shenggui Li, Hongxin Liu, Yukun Zhou, Tianyi Li, and Yang You. Open-sora: Democratizing efficient video production for all. *arXiv preprint arXiv:2412.20404*, 2024. 5
- [55] Jie Zhou, Daniel L Civco, and John A Silander. A wavelet transform method to merge landsat tm and spot panchromatic data. *International journal of remote sensing*, 19(4):743–757, 1998. 1
- [56] Man Zhou, Jie Huang, Yanchi Fang, Xueyang Fu, and Aiping Liu. Pan-sharpening with customized transformer and invertible neural network. In *Proceedings of the AAAI Conference on Artificial Intelligence*, pages 3553–3561, 2022. 2
- [57] Man Zhou, Jie Huang, Keyu Yan, Hu Yu, Xueyang Fu, Aiping Liu, Xian Wei, and Feng Zhao. Spatial-frequency domain information integration for pan-sharpening. In *European Conference on Computer Vision*, pages 274–291. Springer, 2022. 2, 6, 1
- [58] Man Zhou, Keyu Yan, Jie Huang, Zihe Yang, Xueyang Fu, and Feng Zhao. Mutual information-driven pan-sharpening. In *Proceedings of the IEEE/CVF Conference on Computer Vision and Pattern Recognition*, pages 1798–1808, 2022. 1

Cross-Scale Pansharpening via ScaleFormer and the PanScale Benchmark

Supplementary Material

8. Related Work

8.1. Pansharpening

Pan-sharpening methods can generally be categorized into two major paradigms: traditional techniques and deep learning-based approaches. Traditional methods are further divided into three main categories: component substitution (CS) [22, 28], multi-resolution analysis (MRA) [30, 55], and variational optimization (VO) [10, 23]. CS [12, 14] techniques enhance spatial resolution by substituting the spatial textures of the LRMS image with high-frequency details extracted from the PAN image. MRA [36, 40] approaches perform image information through multi-scale fusion, and VO [11, 33] methods generate the HRMS by optimizing the loss function. However, traditional methods typically rely on hand-crafted features and lack robust priors, often resulting in suboptimal results. Driven by the success of deep neural networks, deep learning-based methods have subsequently emerged as the predominant approach in the pan-sharpening community [27, 52, 58]. The pioneering work of PNN [31] initiated the application of convolutional neural networks to pan-sharpening. Following this, research efforts have increasingly focused on devising more sophisticated network architectures (e.g., MSDCNN [50], GPPNN [48]), incorporating auxiliary information (e.g., frequency analysis in SFINet[57] and MSDDN[16]), and exploring innovative learning paradigms [9, 45, 49]. Concurrently, pan-sharpening has witnessed a significant expansion in its richness and diversity. HFIN [38] introduces a hierarchical frequency integration network. Mamba-based methods [4, 34, 46] employ the state-space model to achieve effective pan-sharpening. Furthermore, ARConv [44] presents an adaptive rectangular convolution, enabling the network to learn convolution kernel dimensions tailored to objects of varying scales within remote sensing imagery.

8.2. Scale Generalization in Perceptual Tasks

Scale generalization presents a critical challenge for visual models in perceptual tasks, particularly when dealing with inputs of varying sizes and resolutions. The Flexivit [2] was one of the first attempts to address this issue, enabling the model to adapt to inputs with different patch sizes during training, ensuring stable performance across changing scales. Similarly, Resformer [39] enhances Vision Transformers’ generalization ability in tasks with significant scale variations by employing a multi-resolution training strategy with a scale consistency loss function. Building on this, ViTAR [8] further improves scale generalization by incorporating dynamic resolution adjustments. Additionally, it

introduces fuzzy positional encoding to prevent overfitting to a single resolution. The MSPE [29] method optimizes the patch embedding process with multiple variable-sized patch kernels, pushing the performance of Vision Transformers to new heights, especially in tasks involving multi-scale images, where it demonstrates a substantial improvement in model performance.

9. PanScale Dataset and Benchmark

9.1. Dataset Preprocessing

As is shown in Fig. 7, we first selected 16 geographically diverse regions across the globe, covering a broad spectrum of terrains such as urban, mountainous, oceanic, and desert. This diversity ensures that the resulting dataset effectively captures the challenges of pansharpening under varying environmental conditions, thereby facilitating robust evaluation of model generalization across different geographic contexts. Based on this selection, we sourced imagery from three widely used satellites: Jilin-1, Landsat-9, and Skysat. Taking Landsat imagery as an example, each raw satellite image can be represented as $\mathbf{I} \in \mathbb{R}^{H \times W \times B}$, where H, W , and B denote the height, width, and number of spectral bands. To remove cloud-contaminated pixels, we utilize the quality assessment band Q , which provides metadata indicating the presence of clouds and cirrus. Using this metadata, a binary cloud mask $Mask$ is generated, and the resulting cloud-free image is defined as:

$$\mathbf{I}' = \mathbf{I} \odot Mask \quad (12)$$

Building upon the cloud-free images, we collect all available Landsat satellite observations covering a selected geographic region within a defined time interval $[t_0, t_1]$, resulting in an image set:

$$\mathcal{I} = \{\mathbf{I}'_1, \mathbf{I}'_2, \dots, \mathbf{I}'_N\} \quad (13)$$

For each spectral band $b \in [1, B]$, we perform a pixel-wise median compositing across all cloud-free images in the set \mathcal{I} to generate a temporally stable and noise-reduced composite band:

$$\mathbf{I}_b^{mid}(i, j) = median(\{\mathbf{I}_{1,b}(i, j), \mathbf{I}_{2,b}(i, j), \dots, \mathbf{I}_{N,b}(i, j)\}) \quad (14)$$

where (i, j) denotes the spatial pixel location with $i \in [1, H]$ and $j \in [1, W]$. By stacking the median composites of all spectral bands, we obtain the final multi-band synthesized image, denoted as \mathbf{I}^{med} . Leveraging the band extraction and export capabilities of Google Earth Engine, we further derive the corresponding panchromatic (PAN) images and

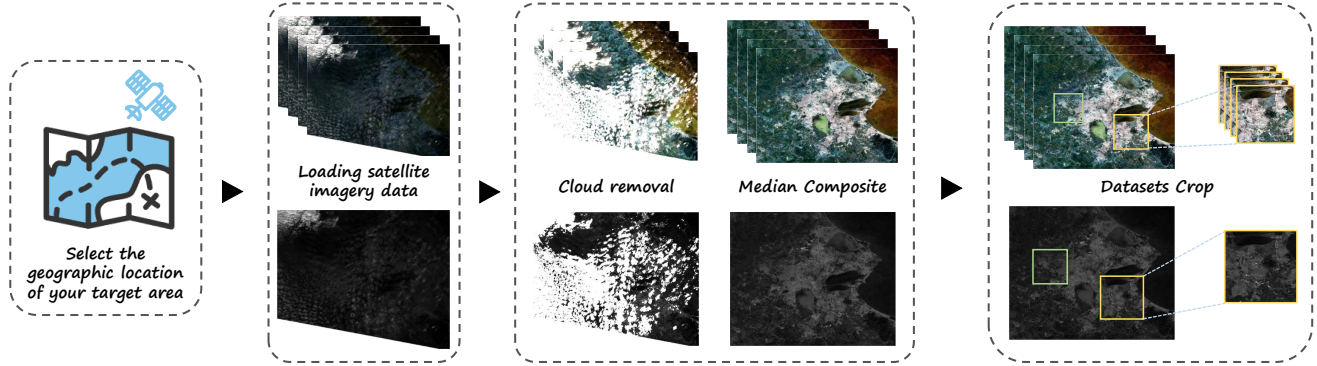


Figure 7. The construction pipeline of the PanScale dataset, which consists of three main stages: accessing satellite imagery via Google Earth Engine, data preprocessing, and data cropping.

low-resolution multi-spectral (LRMS) images for subsequent use in pansharpening.

9.2. Dataset Construction

Table 6 presents the detailed configuration of the dataset construction. The training sets for the three constituent sources—Jilin-1, Landsat-9, and Skysat—are designed with distinct upsampling ratios of $4\times$, $2\times$, and $2.5\times$, respectively. This variation in scaling allows the models to be exposed to diverse resolution levels during training.

For a comprehensive evaluation, we establish a multi-resolution testing framework to rigorously assess the cross-scale generalization ability of pansharpening models. Specifically, the reduced-resolution (RR) testing sets consist of images at resolutions of 1600×1600 , 800×800 , 400×400 , and 200×200 pixels. Notably, for the Jilin dataset, the maximum available resolution is 800×800 , and therefore, the 1600×1600 variant is not included. In addition to the RR evaluations, we provide full-resolution (FR) test sets at varying scales to further evaluate model robustness across real-world spatial variations.

9.3. Benchmark Design

To comprehensively evaluate diverse methods on the PanScale benchmark, we employ a suite of image quality assessment (IQA) metrics. Specifically, we select six prevalent reference-based metrics: Peak Signal-to-Noise Ratio (PSNR) [18], Structural Similarity Index (SSIM) [47], Spectral Angle Mapper (SAM) [51], Relative Dimensionless Global Error in Synthesis (ERGAS) [43], Spatial Correlation Coefficient (SCC) [19] and Quality index (Q) [42]. PSNR and SSIM primarily quantify spatial fidelity, with higher values indicating superior preservation of spatial details. Conversely, SAM and ERGAS focus on assessing spectral accuracy, where lower values denote diminished spectral distortion and enhanced consistency with the reference data. SCC assesses the spatial correlation between images, while Q provides a

comprehensive measure of universal image quality for pansharpened MS images. Furthermore, to provide additional evaluation of model performance on PanScale, we also leverage three reference-free IQA metrics that do not rely on ground truth data. These include the spectral distortion index D_λ [20], the spatial distortion index D_S , and the Quality with No Reference (QNR) [1]. Specifically, D_λ and D_S quantify the extent of spectral and spatial distortion, respectively. QNR provides a holistic assessment of image quality without reference.

10. Additional experimental results

10.1. More Visual Comparison

Due to space constraints, we provide only the visualization results for the Jilin dataset in the main text. More visual comparison results for the three datasets are shown in Fig. 8, 9, and 10. The zoomed-in comparison images and corresponding MSE maps demonstrate that the proposed method excels in preserving fine details and spectral fidelity. These results highlight its strong adaptability to large-scale pansharpening tasks, showcasing its ability to handle high-resolution image fusion effectively.

10.2. Comprehensive Quantitative Comparison

Due to space limitations, we report only the average multi-scale performance on the reduced resolution datasets in Table 2 of the main text. For completeness and reproducibility, the full quantitative results across all resolutions and datasets are provided in the following tables: Table 7 (Jilin dataset at 200 and 400 resolutions), Table 8 (Jilin dataset at 800 resolution), Table 9 (Landsat dataset at 200 and 400 resolutions), Table 10 (Landsat dataset at 800 and 1600 resolutions), Table 11 (Skysat dataset at 200 and 400 resolutions), and Table 12 (Skysat dataset at 800 and 1600 resolutions). These results offer a more detailed perspective on the performance of each method across different scales. Notably,

Table 6. Detailed Information of the PanScale Datasets, where "samples" denotes the number of samples at each scale, "scale" represents the height or width of the square PAN image, and "res" indicates the image resolution used for dataset creation.

	Jilin (4×)			Landsat (2×)			Skysat (2.5×)		
	Samples	Scale	Res(m)	Samples	Scale	Res(m)	Samples	Scale	Res(m)
Train	1055	200	2	2484	256	30	2370	200	2
RR Test	34	800,400 200	2	96	1600,800 400,200	30	88	1600,800 400,200	2
FR Test	121	2000,1600 1200,800	2	48	2000,1600 1200,800	30	34	2000,1600 1200,800	2

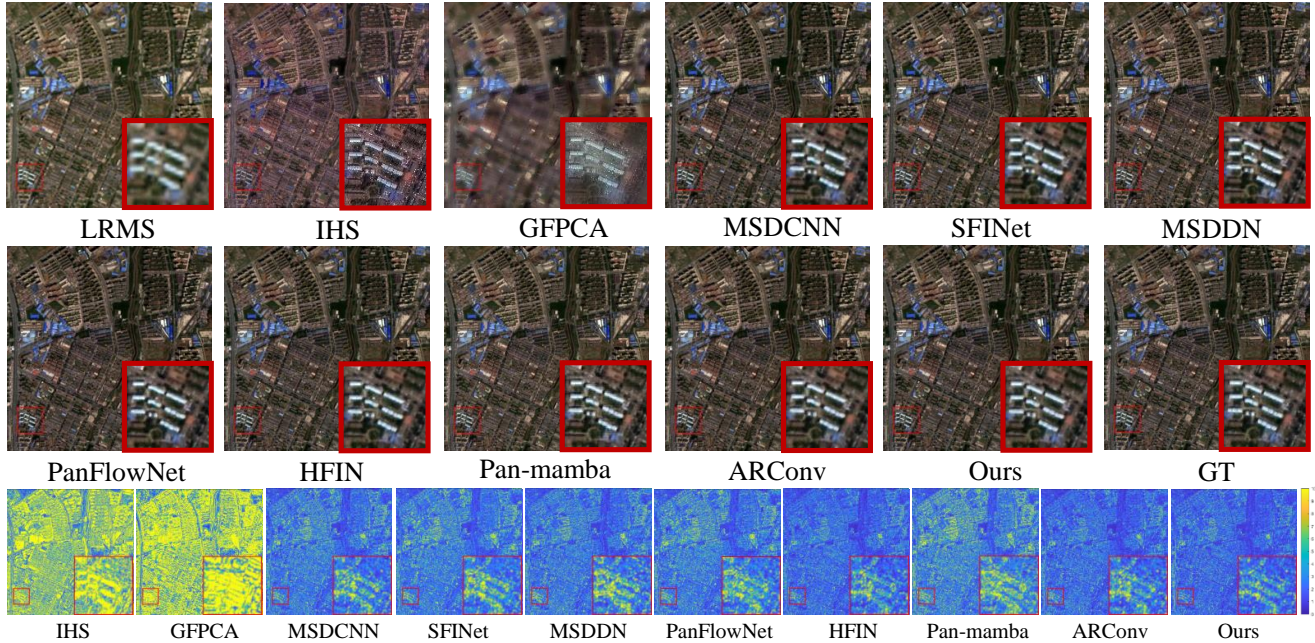


Figure 8. Comparative visual experiments of several methods on Jilin datasets.

our proposed method consistently outperforms existing approaches across nearly all metrics, demonstrating its superior cross-scale generalization capability.

Similarly, for the full-resolution experiments summarized in Table 3 of the main text, we report only the averaged results across multiple scales. To ensure completeness and facilitate further analysis, the detailed performance metrics for each resolution are presented in the following supplementary tables: Table 13 (Full Jilin dataset at 800, 1200, 1600, and 2000 resolutions), Table 14 (Full Landsat dataset at 800, 1200, 1600, and 2000 resolutions), and Table 15 (Full Skysat dataset at 800, 1200, 1600, and 2000 resolutions). These comprehensive results show that our method achieves performance on par with or superior to state-of-the-art techniques even under full-resolution settings, demonstrating strong generalization capability across scales in real-world scenarios.

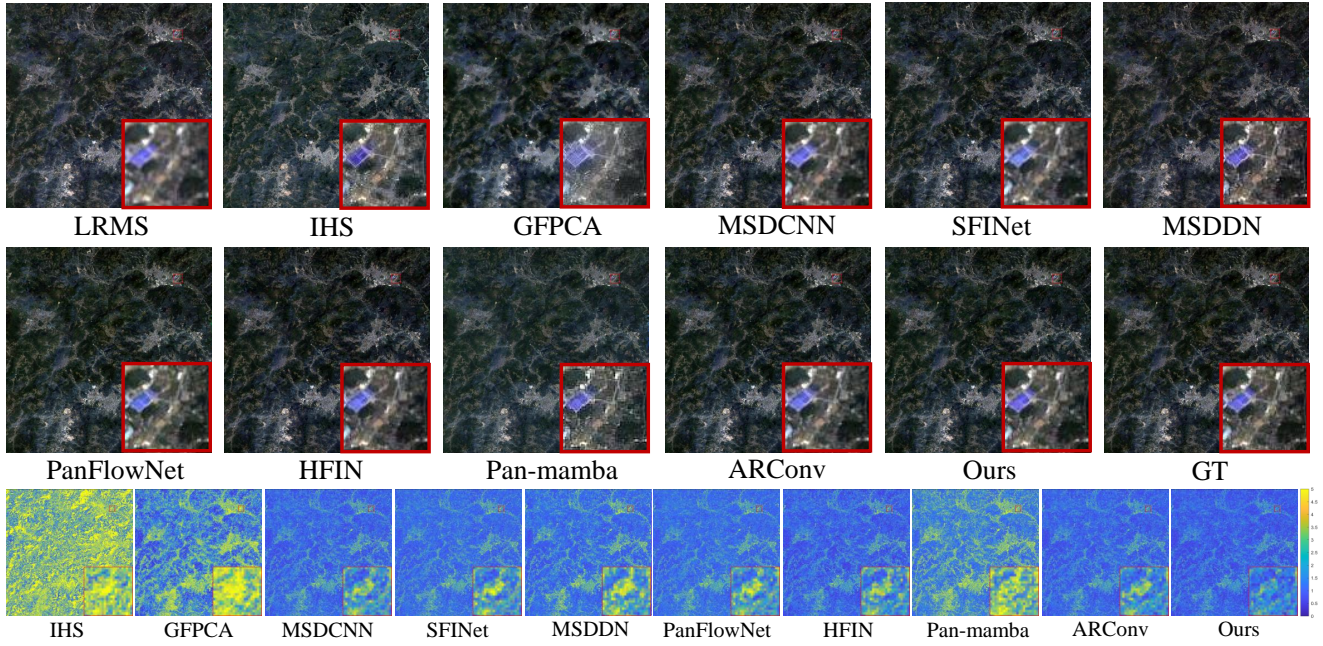


Figure 9. Comparative visual experiments of several methods on Landsat datasets.

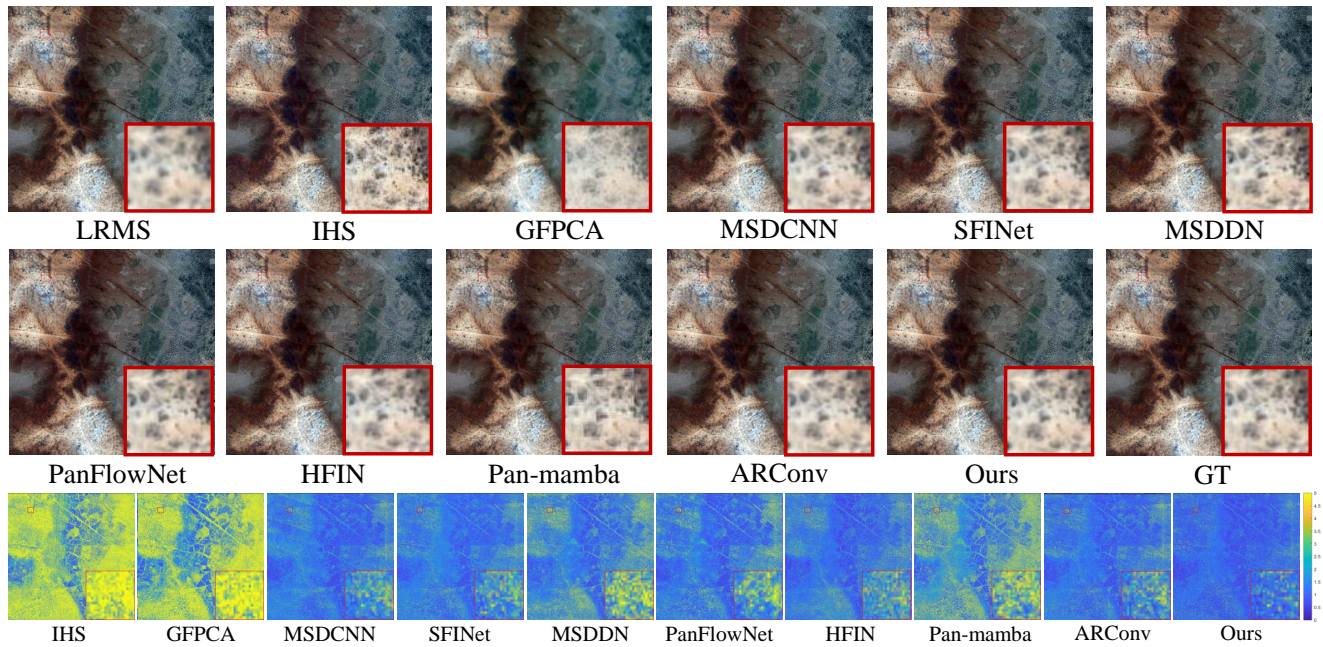


Figure 10. Comparative visual experiments of several methods on Skysat datasets.

Table 7. Multi-resolution results on the Jilin datasets (Part 1), with numbers indicating the size of the PAN image. The best are highlighted in **bold**.

Method	Jilin-200						Jilin-400					
	PSNR \uparrow	SSIM \uparrow	SAM \downarrow	ERGAS \downarrow	SCC \uparrow	Q \uparrow	PSNR \uparrow	SSIM \uparrow	SAM \downarrow	ERGAS \downarrow	SCC \uparrow	Q \uparrow
GS	25.7681	0.7128	0.0573	5.3592	0.8592	0.6002	25.6914	0.7099	0.0570	5.5151	0.8683	0.5805
IHS	25.9327	0.7081	0.0590	5.6410	0.8488	0.5930	25.8671	0.7063	0.0588	5.7120	0.8618	0.5754
GFPCA	25.6482	0.7106	0.0761	5.1018	0.8730	0.4579	25.8554	0.7252	0.0733	4.9484	0.8882	0.4469
MSDCNN	36.5984	0.9555	0.0277	1.5336	0.9885	0.9146	37.0869	0.9588	0.0265	1.4275	0.9907	0.9056
SFINet	36.2407	0.9508	0.0306	1.6494	0.9872	0.9017	36.6916	0.9532	0.0301	1.5592	0.9895	0.8915
MSDDN	37.5748	0.9653	0.0242	1.3600	0.9910	0.9289	37.7031	0.9667	0.0244	1.3366	0.9922	0.9174
PanFlowNet	36.6522	0.9571	0.0277	1.5303	0.9886	0.9163	36.8303	0.9583	0.0272	1.4832	0.9903	0.9038
HFIN	38.0366	0.9686	0.0228	1.3103	0.9919	0.9343	38.2695	0.9693	0.0224	1.2464	0.9932	0.9223
Pan-mamba	36.1465	0.9517	0.0278	1.6057	0.9873	0.9092	36.3710	0.9534	0.0280	1.5434	0.9891	0.8985
ARConv	38.1115	0.9682	0.0233	1.2904	0.9919	0.9338	38.5962	0.9701	0.0225	1.2113	0.9934	0.9246
Ours	39.3300	0.9759	0.0202	1.1152	0.9941	0.9449	39.6334	0.9762	0.0197	1.0728	0.9950	0.9336

Table 8. Multi-resolution results on the Jilin datasets (Part 2), with numbers indicating the size of the PAN image. The best are highlighted in **bold**.

Method	Jilin-800					
	PSNR \uparrow	SSIM \uparrow	SAM \downarrow	ERGAS \downarrow	SCC \uparrow	Q \uparrow
GS	24.8563	0.6939	0.0605	5.9530	0.8700	0.5739
IHS	24.9852	0.6926	0.0611	6.0682	0.8659	0.5726
GFPCA	25.3367	0.7198	0.0738	5.0877	0.8974	0.4479
MSDCNN	36.0279	0.9578	0.0263	1.5284	0.9907	0.9074
SFINet	35.9211	0.9528	0.0295	1.6301	0.9901	0.8942
MSDDN	35.5442	0.9617	0.0266	1.6012	0.9903	0.9122
PanFlowNet	35.5154	0.9543	0.0278	1.6527	0.9897	0.9001
HFIN	37.6967	0.9714	0.0219	1.2696	0.9940	0.9285
Pan-mamba	34.1367	0.9388	0.0311	1.9399	0.9858	0.8822
ARConv	37.9942	0.9708	0.0221	1.2368	0.9940	0.9288
Ours	38.9161	0.9762	0.0196	1.1093	0.9953	0.9369

Table 9. Multi-resolution results on the Landsat datasets (Part 1), with numbers indicating the size of the PAN image. The best are highlighted in **bold**.

Method	Landsat-200						Landsat-400					
	PSNR \uparrow	SSIM \uparrow	SAM \downarrow	ERGAS \downarrow	SCC \uparrow	Q \uparrow	PSNR \uparrow	SSIM \uparrow	SAM \downarrow	ERGAS \downarrow	SCC \uparrow	Q \uparrow
GS	36.6649	0.9049	0.0413	4.1725	0.8227	0.5872	36.1124	0.8994	0.0481	4.0663	0.8504	0.5853
IHS	37.3551	0.9001	0.0364	4.1847	0.7969	0.5566	36.7972	0.8952	0.0398	4.0051	0.8263	0.5547
GFPCA	37.1018	0.8968	0.0432	3.7622	0.8255	0.4707	36.9330	0.8975	0.0431	3.3999	0.8967	0.4744
MSDCNN	38.8386	0.9590	0.0407	2.8789	0.8242	0.6667	38.6542	0.9597	0.0396	2.7907	0.8442	0.6678
SFINet	38.7072	0.9523	0.0486	3.3100	0.8428	0.6666	39.1371	0.9569	0.0484	2.7937	0.8649	0.6683
MSDDN	37.8541	0.9360	0.0609	3.2539	0.8212	0.6442	38.3405	0.9391	0.0524	2.7208	0.8213	0.6433
PanFlowNet	37.9274	0.9343	0.0721	3.8958	0.8263	0.6571	38.3768	0.9423	0.0627	3.3714	0.8470	0.6592
HFIN	39.9710	0.9635	0.0345	2.8424	0.8768	0.7165	40.6129	0.9698	0.0337	2.2585	0.9031	0.7208
Pan-mamba	39.505	0.9553	0.0530	3.0258	0.8701	0.7093	38.7678	0.9471	0.0487	2.6194	0.8512	0.6703
ARConv	39.6267	0.9624	0.0365	2.8184	0.8411	0.6770	39.8234	0.9645	0.0368	2.4587	0.8713	0.6812
Ours	40.6063	0.9677	0.0341	2.6561	0.8869	0.7317	41.3715	0.9725	0.0333	2.1051	0.9081	0.7367

Table 10. Multi-resolution results on the Landsat datasets (Part 2), with numbers indicating the size of the PAN image. The best are highlighted in **bold**.

Method	Landsat-800						Landsat-1600					
	PSNR↑	SSIM↑	SAM↓	ERGAS↓	SCC ↑	Q ↑	PSNR↑	SSIM↑	SAM↓	ERGAS↓	SCC ↑	Q ↑
GS	34.9034	0.8949	0.0517	4.6372	0.8873	0.5911	32.6318	0.8817	0.0633	5.5056	0.9064	0.5857
IHS	35.6661	0.8915	0.0407	4.2507	0.8640	0.5616	33.6923	0.8791	0.0461	4.8532	0.8755	0.5486
GFPCA	36.1215	0.8963	0.0413	3.5643	0.9074	0.4790	34.8823	0.8946	0.0418	3.6901	0.9320	0.4748
MSDCNN	38.7256	0.9600	0.0388	2.6008	0.8973	0.6809	39.0508	0.9582	0.0430	2.3577	0.9553	0.6792
SFINet	39.1135	0.9575	0.0461	2.5864	0.9167	0.6804	38.3526	0.9600	0.0389	2.5399	0.9314	0.6803
MSDDN	37.7455	0.9364	0.0506	2.7781	0.8704	0.6480	36.8196	0.9269	0.0515	2.8563	0.9072	0.6329
PanFlowNet	38.2522	0.9438	0.0573	3.1225	0.8994	0.6735	38.3067	0.9527	0.0475	2.6904	0.9453	0.6777
HFIN	40.2656	0.9664	0.0343	2.1820	0.9429	0.7249	39.9946	0.9665	0.0349	2.0090	0.9701	0.7243
Pan-mamba	35.7809	0.9131	0.0579	3.2307	0.8508	0.6291	32.8549	0.8668	0.0744	4.1172	0.8376	0.5661
ARConv	39.7381	0.9642	0.0342	2.3293	0.9185	0.6943	39.4700	0.9642	0.0339	2.1698	0.9511	0.6939
Ours	41.1326	0.9719	0.0327	1.9870	0.9471	0.7438	41.0335	0.9722	0.0317	1.7934	0.9735	0.7458

Table 11. Multi-resolution results on the Skysat datasets (Part 1), with numbers indicating the size of the PAN image. The best are highlighted in **bold**.

Method	Skysat-200						Skysat-400					
	PSNR↑	SSIM↑	SAM↓	ERGAS↓	SCC ↑	Q ↑	PSNR↑	SSIM↑	SAM↓	ERGAS↓	SCC ↑	Q ↑
GS	39.4693	0.9354	0.0326	2.2604	0.9121	0.6343	39.2596	0.9346	0.0310	2.3096	0.9357	0.6478
IHS	40.1768	0.9354	0.0264	2.0909	0.8934	0.6259	39.7388	0.9326	0.0260	2.1468	0.9206	0.6362
GFPCA	38.0562	0.9289	0.0454	2.4658	0.8896	0.4720	37.8788	0.9275	0.0441	2.4482	0.9213	0.4867
MSDCNN	43.0041	0.9758	0.0406	2.8975	0.8886	0.7373	43.1001	0.9788	0.0399	2.2283	0.9259	0.7450
SFINet	41.6073	0.9417	0.1010	3.4414	0.8496	0.6763	41.3735	0.9418	0.0939	3.1682	0.8911	0.6829
MSDDN	42.3969	0.9462	0.0825	2.9244	0.8947	0.7115	41.7617	0.9489	0.0697	2.7420	0.9243	0.7096
PanFlowNet	41.0920	0.9484	0.0757	3.2361	0.8467	0.6674	40.9916	0.9508	0.0667	2.9674	0.9009	0.6703
HFIN	43.7949	0.9533	0.0749	2.6743	0.9073	0.7637	43.9910	0.9669	0.0561	2.2725	0.9443	0.7758
Pan-mamba	43.2983	0.9516	0.0908	2.8129	0.8955	0.7546	42.7551	0.9590	0.0679	2.5895	0.9298	0.7461
ARConv	43.5032	0.9785	0.0423	2.1815	0.8934	0.7475	43.4617	0.9795	0.0406	2.0500	0.9344	0.7596
Ours	44.9275	0.9826	0.0362	1.7945	0.9339	0.7837	44.6718	0.9824	0.0364	1.7266	0.9519	0.7874

Table 12. Multi-resolution results on the Skysat datasets (Part 2), with numbers indicating the size of the PAN image. The best are highlighted in **bold**.

Method	Skysat-800						Skysat-1600					
	PSNR↑	SSIM↑	SAM↓	ERGAS↓	SCC ↑	Q ↑	PSNR↑	SSIM↑	SAM↓	ERGAS↓	SCC ↑	Q ↑
GS	38.9661	0.9302	0.0322	2.4344	0.9474	0.6367	38.5282	0.9264	0.0328	2.4648	0.9555	0.6294
IHS	39.3872	0.9280	0.0275	2.2406	0.9361	0.6247	39.0572	0.9255	0.0269	2.2241	0.9468	0.6217
GFPCA	37.4581	0.9282	0.0457	2.5427	0.9345	0.4751	37.2721	0.9272	0.0446	2.5326	0.9442	0.4755
MSDCNN	43.0467	0.9792	0.0391	2.1924	0.9347	0.7424	40.9681	0.9444	0.0851	3.0750	0.9211	0.6798
SFINet	41.3829	0.9452	0.0813	2.9911	0.9136	0.6787	42.6192	0.9786	0.0391	2.3726	0.9423	0.7419
MSDDN	40.7615	0.9475	0.0652	2.7640	0.9327	0.6900	39.2365	0.9397	0.0691	2.9878	0.9323	0.6684
PanFlowNet	41.1307	0.9558	0.0609	2.7860	0.9215	0.6733	40.8734	0.9570	0.0598	2.7015	0.9393	0.6801
HFIN	44.2075	0.9714	0.0508	2.0866	0.9581	0.7725	43.8435	0.9716	0.0516	2.0618	0.9680	0.7709
Pan-mamba	40.9513	0.9527	0.0626	2.6565	0.9320	0.7017	38.5358	0.9340	0.0689	3.0077	0.9245	0.6491
ARConv	43.4413	0.9803	0.0398	2.0106	0.9470	0.7594	43.2087	0.9806	0.0391	2.0094	0.9529	0.7591
Ours	44.7328	0.9830	0.0356	1.6606	0.9613	0.7819	44.6416	0.9829	0.0347	1.7355	0.9686	0.7811

Table 13. Multi-resolution results on the Full-Jilin datasets, with numbers indicating the size of the PAN image. The best are highlighted in **bold**, and the second are underlined.

Method	Full-Jilin-800			Full-Jilin-1200			Full-Jilin-1600			Full-Jilin-2000		
	$D_\lambda \downarrow$	$D_S \downarrow$	QNR \uparrow	$D_\lambda \downarrow$	$D_S \downarrow$	QNR \uparrow	$D_\lambda \downarrow$	$D_S \downarrow$	QNR \uparrow	$D_\lambda \downarrow$	$D_S \downarrow$	QNR \uparrow
GS	0.0795	0.1936	0.7433	0.0791	0.2012	0.7362	0.0814	0.2055	0.7304	0.0846	0.2081	0.7253
IHS	0.0955	0.2060	0.7191	0.0961	0.2121	0.7126	0.0972	0.2150	0.7092	0.0997	0.2165	0.7056
GFPCA	<u>0.0464</u>	0.1001	0.8584	0.0420	0.0980	0.8641	0.0405	0.0980	0.8654	0.0407	0.0979	0.8654
MSDCNN	0.0537	0.0499	0.8995	0.0460	<u>0.0416</u>	0.9144	0.0455	<u>0.0394</u>	0.9170	0.0454	0.0371	0.9194
SFINet	0.0596	0.0515	0.8925	0.0519	0.0430	0.9075	0.0517	0.0415	0.9092	0.0519	0.0395	0.9109
MSDDN	0.0481	0.0521	<u>0.9046</u>	<u>0.0398</u>	0.0509	0.9118	0.0387	0.0521	0.9116	0.0394	0.0533	0.9106
PanFlowNet	0.0502	0.0438	0.9044	0.0455	0.0384	<u>0.9179</u>	0.0441	0.0364	0.9201	0.0439	0.0340	0.9196
HFIN	0.0479	0.0522	0.9030	0.0414	0.0470	0.9138	0.0403	0.0453	0.9164	0.0398	0.0437	0.9182
Pan-mamba	0.0516	0.0501	0.9013	0.0446	0.0427	0.9148	0.0447	0.0402	<u>0.9171</u>	0.0450	0.0373	<u>0.9195</u>
ARConv	0.0468	0.0656	0.8907	0.0407	0.0629	0.8989	0.0398	0.0619	0.9007	<u>0.0396</u>	0.0611	0.9016
Ours	0.0454	<u>0.0476</u>	0.9077	0.0394	0.0428	0.9181	<u>0.0394</u>	0.0405	0.9177	0.0393	<u>0.0363</u>	0.9189

Table 14. Multi-resolution results on the Full-Landsat datasets, with numbers indicating the size of the PAN image. The best are highlighted in **bold**, and the second are underlined.

Method	Full-Landsat-800			Full-Landsat-1200			Full-Landsat-1600			Full-Landsat-2000		
	$D_\lambda \downarrow$	$D_S \downarrow$	QNR \uparrow	$D_\lambda \downarrow$	$D_S \downarrow$	QNR \uparrow	$D_\lambda \downarrow$	$D_S \downarrow$	QNR \uparrow	$D_\lambda \downarrow$	$D_S \downarrow$	QNR \uparrow
GS	0.0519	0.1145	0.8405	0.0589	0.1155	0.8334	0.0567	0.1076	0.8425	0.0598	0.1064	0.8406
IHS	0.0862	0.1235	0.8012	0.0972	0.1286	0.7883	0.0982	0.1205	0.7945	0.1028	0.1205	0.7905
GFPCA	0.0731	0.0577	0.8737	0.0623	0.0543	0.8870	0.0627	0.0525	0.8883	0.0615	0.0510	0.8910
MSDCNN	0.0523	0.0378	0.9135	0.0476	0.0316	0.9234	0.0485	0.0307	0.9234	0.0468	0.0303	0.9254
SFINet	0.0493	0.0405	0.9137	0.0410	0.0331	0.9278	0.0404	0.0314	0.9299	0.0392	0.0317	0.9307
MSDDN	0.0402	0.0246	0.9372	0.0311	<u>0.0224</u>	0.9477	0.0317	0.0229	0.9466	0.0312	0.0246	0.9454
PanFlowNet	0.0570	0.0388	0.9077	0.0449	<u>0.0379</u>	0.9194	0.0458	0.0385	0.9178	0.0449	0.0384	0.9187
HFIN	0.0287	0.0200	<u>0.9523</u>	0.0228	0.0201	0.9543	<u>0.0229</u>	0.0188	0.9590	<u>0.0217</u>	<u>0.0198</u>	<u>0.9591</u>
Pan-mamba	0.0295	0.0525	0.9196	0.0297	0.0675	<u>0.9049</u>	0.0312	0.0816	0.8898	0.0330	0.0928	0.8773
ARConv	<u>0.0278</u>	<u>0.0231</u>	0.9501	0.0260	0.0200	0.9548	0.0251	<u>0.0191</u>	0.9566	0.0239	0.0183	0.9585
Ours	0.0272	0.0271	0.9537	<u>0.0240</u>	0.0225	0.9563	0.0217	0.0209	<u>0.9580</u>	0.0206	0.0206	0.9594

Table 15. Multi-resolution results on the Full-Skysat datasets, with numbers indicating the size of the PAN image. The best are highlighted in **bold**, and the second are underlined.

Method	Full-Skysat-800			Full-Skysat-1200			Full-Skysat-1600			Full-Skysat-2000		
	$D_\lambda \downarrow$	$D_S \downarrow$	QNR \uparrow	$D_\lambda \downarrow$	$D_S \downarrow$	QNR \uparrow	$D_\lambda \downarrow$	$D_S \downarrow$	QNR \uparrow	$D_\lambda \downarrow$	$D_S \downarrow$	QNR \uparrow
GS	0.0533	0.1033	0.8499	0.0657	0.1163	0.8273	0.0653	0.1129	0.8304	0.0649	0.1123	0.8311
IHS	0.0937	0.1282	0.7916	0.0973	0.1343	0.7834	0.0993	0.1333	0.7822	0.0994	0.1314	0.7836
GFPCA	0.0427	0.0633	0.8974	0.0445	0.0633	0.8956	0.0428	0.0620	0.8983	0.0432	0.0610	0.8989
MSDCNN	0.0449	0.0262	<u>0.9344</u>	0.0407	<u>0.0282</u>	<u>0.9422</u>	0.0422	0.0187	<u>0.9391</u>	0.0398	0.0155	0.9455
SFINet	0.1357	0.0331	0.8373	0.1304	0.0343	0.8412	0.1363	0.0333	0.8362	0.1361	0.0327	0.8368
MSDDN	<u>0.0424</u>	0.0386	0.9217	<u>0.0388</u>	0.0382	0.9250	0.0426	0.0355	0.9294	0.0408	0.0327	0.9293
PanFlowNet	0.0883	0.0376	0.8787	0.0761	0.0339	0.8935	0.0738	0.0312	0.8981	0.0726	0.0301	0.9003
HFIN	0.0623	0.0634	0.8796	0.0583	0.0573	0.8888	0.0584	0.0588	0.8872	0.0572	0.0565	0.8904
Pan-mamba	0.0579	0.0383	0.9071	0.0546	0.0330	0.9152	0.0515	0.0284	0.9224	0.0491	<u>0.0248</u>	0.9279
ARConv	0.0405	0.0416	0.9201	0.0381	0.0402	0.9237	0.0380	0.0415	0.9225	<u>0.0380</u>	0.0404	0.9236
Ours	0.0451	<u>0.0292</u>	0.9365	0.0423	0.0248	0.9425	<u>0.0407</u>	<u>0.0269</u>	0.9426	0.0339	0.0268	<u>0.9416</u>